Dual-Emissive Persistent Luminescence Nanoparticle-Based Charge-Reversible Intelligent Nanoprobe for Persistent Luminescence-Ratio Bioimaging along with Chemo-Photothermal Synergic Therapy

Jia-Lin Liu, Xu Zhao,* Li-Jian Chen, Lu-Ming Pan, and Xiu-Ping Yan*

ACCESS | 📊 Metrics & More | 📰 Article Recommendations | 🔲 Supporting Information

ABSTRACT: Persistent luminescence nanoparticles (PLNPs) hold great promise for bioimaging owing to no demand for *in situ* excitation and negligible tissue autofluorescence interference. Nevertheless, huge challenges remain in the further development of single-emissive PLNPs due to the great variation of luminescence with time after excitation ceases. Herein, we report the controllable fabrication of dual-emissive monodispersed PLNPs ($ZnGa_2O_4$:Cr) by a surfactant-assisted hydrothermal method in combination with postcalcination for bioimaging. The prepared PLNPs emit luminescence at 508 and 714 nm with a constant luminescence ratio (I_{508}/I_{714}) for more than 1 h after UV excitation stops. Moreover, the prepared PLNPs give a constant I_{508}/I_{714} ratio signal after repeated excitation by a LED lamp, allowing luminescence ratio imaging to ensure the long-term accuracy for *in vivo* imaging. *In vivo* ratio imaging demonstrates the potential of the prepared PLNPs for precision bioimaging. In addition, the prepared PLNPs have been applied to fabricate a theranostic nanoprobe with intelligent tumor-targeted imaging and chemo-photothermal synergistic therapy to further reveal their unique advantage for imaging guided therapy. We believe that the dual-emissive PLNPs will provide a promising nanoplatform for bioimaging and biomedical applications.
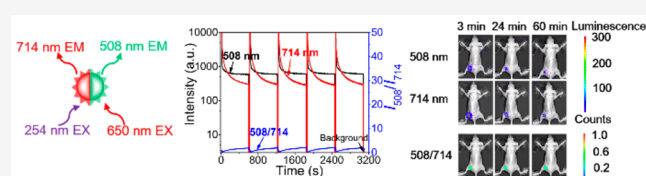
INTRODUCTION

Cancer is a serious threat to human survival and social development, and its incidence and mortality are increasing year by year. The development of imaging technology is of great significance for real-time monitoring of cancer progression and further investigation of cancer biology at the cell level.[1,2] Optical imaging has attracted increasing attention because of its inherent short response time, high sensitivity, and temporal−spatial resolution.[3−5] However, traditional optical reagents such as organic fluorescent probes and inorganic fluorescent nanoparticles are often subject to the interference of autofluorescence, photobleaching, or phototoxicity.[6] Persistent luminescence nanoparticles (PLNPs), a magical optical material, can store excitation energy and slowly release it in the form of persistent luminescence after excitation stops.[7−9] The feature of *in situ* excitation-free luminescence gives PLNPs an outstanding advantage of no tissue autofluorescence interference for *in vivo* imaging.[10,11] However, current PLNPs are limited to single-wavelength emission and are susceptible to a luminescence variation with time after stopping excitation, which has impeded the further development of PLNPs in bioimaging.[12,13] A dual-emissive probe can perform self-calibration reading and ratio imaging by detecting the fluorescence intensities at two different wavelengths, thereby effectively avoiding the interference of external factors. Dual-emissive PLNPs, therefore, are expected to achieve

constant ratio imaging with a long detection window, promoting the biomedical applications of PLNPs.

Various therapeutic strategies based on different mechanisms have been developed for cancer therapy.[14−16] However, a single modal therapy is incapable of eradicating tumors due to the intrinsic defects of each treatment method and the complex tumor microenvironment.[17,18] Synergistic therapy, integrated with two or more treatments, is a promising alternative therapeutic technique, which can achieve super-additive therapeutic effects.[19,20] For example, the combination of photothermal therapy and chemotherapy holds tremendous promise in improving therapeutic efficiency and reducing side effects by controlling the drug release strategy under specific stimuli of a tumor.[21,22]

Targeting is also the key to improving the efficiency of imaging and treatment.[23] However, the conventional targeting strategy mainly relies on the interaction between a specific ligand and the tumor receptor, which easily causes a negative effect on the heterogeneity of malignant tumors.[24] On the basis of the acidic microenvironment of tumor issues, an intelligent
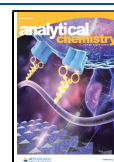
charge-switchable "smart" targeting strategy is a promising alternative approach to the demands of tumor-specific targeting and blood circulation.[25−27]

Herein, we report the controllable fabrication of dual-emissive monodispersed PLNP ($ZnGa_2O_4$:Cr) for persistent luminescence-ratio bioimaging as well as the rational design of a dual-emissive PLNP-based charge-reversible intelligent theranostic nanoprobe for imaging-guided chemo-photo-thermal (chemo-PTT) synergic therapy. A surfactant-aided hydrothermal synthesis in combination with postcalcination is developed to prepare dual-emissive PLNP $ZnGa_2O_4$:Cr with two emission peaks at 508 and 714 nm and a constant ratio signal (I_{508}/I_{714}) in a long time window. A polydopamine (PDA) layer is grown on the surface of the PLNP to prepare PLNP@PDA via the strong adhesion of dopamine. To improve the stability and biocompatibility and offer the charge-reversible intelligent targeting ability, N-hydroxysuccinimide (NHS) and 2,3-dimethylmaleic anhydride (DMMA) functionalized polyethylene glycol (PEG) (NHS-PEG-DMMA) is further introduced on the surface of PLNP@PDA through a condensation reaction. The resulting PLNP@PDA@DMMA is used to load doxorubicin hydrochloride (DOX·HCl) by $\pi-\pi$ stacking and electrostatic adsorption to construct the final chemo-PTT synergic theranostic nanoprobe PLNP@PDA@DMMA/DOX. The as-synthesized theranostic nanoprobe not only shows precision tumor-targeting luminescence-ratio imaging with a long detection window but also possesses enhanced chemo-PTT synergetic therapeutic effects, holding great potential in practical applications.

■ EXPERIMENTAL SECTION

Synthesis of Dual-Emissive PLNPs. A 6.4 mg amount of cetyltrimethylammonium bromide (CTAB) was placed in ultrapure water and dispersed ultrasonically until the solution was clear. $Ga(NO_3)_3$, $Zn(NO_3)_2$·$6H_2O$, and $Cr(NO_3)_3$·$9H_2O$ were added to the above solution in turn with vigorous stirring according to the mole ratio Zn:Ga:O:Cr = 1:2:4:x (x = 0.004, 0.0016, 0.0004, 0.0002, 0.0001, and 0.00008, respectively). The pH of the mixture was adjusted to 8.0 with ammonia solution. The reaction solution was ultrasonicated at room temperature for 30 min and was stirred for a further 1.5 h. The turbid solution was transferred into a 50 mL Teflon-lined stainless steel autoclave and then heated at 220 °C for a certain period of time (12, 24, 36, and 48 h, respectively) for the hydrothermal reaction and cooled to room temperature. The resulting solution was centrifuged at 10000 rpm for 10 min and washed sequentially with ultrapure water and ethanol and then lyophilized. The dried white powder was sintered in a muffle furnace for 1 h at a certain temperature (600, 800, and 1000 °C, respectively).

Synthesis of PLNP@PDA@DMMA. Hydroxylation was performed after wet-grinding by ultrasonic treatment of the PLNP powder (400 mg) in NaOH solution (5 mmol L^{-1}) for 30 min. After vigorous stirring for 24 h, the supernatant was collected after centrifugation at 10000 rpm for 10 min to acquire PLNP-OH. A 20 mL portion of PLNP-OH (1 mg mL^{-1}) in Tris-HCl buffer (pH 8.5, 10 mmol L^{-1}) was mixed with 1.4 mL of dopamine (1 mg mL^{-1}) in Tris-HCl buffer (pH 8.5, 10 mmol L^{-1}). The resulting solution was stirred at room temperature for a certain time (0.5, 1.0, 1.5, and 2.0 h, respectively), followed by centrifugation at 10000 rpm for 5 min. The resulting PLNP@PDA was resuspended in 20 mL of

ultrapure water. Two more centrifugation−redispersion cycles were needed to give PLNP@PDA.

A 350 mg amount of PLNP@PDA was dispersed in Tris-HCl buffer (pH 8.5, 10 mmol L^{-1}, 350 mL). A 1.5 mL portion of ethylenediamine (EDA) was added to the above suspension and the mixture stirred in the dark at room temperature for 24 h. The product was collected by centrifugation and washed with ultrapure water several times to remove residual reactants and then lyophilized to give PLNP@PDA-NH_2.

A 25 mg amount of PLNP@PDA-NH_2 was dissolved in a round-bottom flask containing 22 mL of phosphate-buffered saline (PBS, pH 7.4, 10 mmol·L^{-1}) under ultrasonication, and then an excess of N,N-diisopropylethylamine (DIPEA) was added. At the same time, NHS-PEG-DMMA (50 mg) dispersed in 3 mL of the same PBS was slowly added, and the mixture was then stirred at room temperature overnight. The resulting solid was collected via centrifugation at 10000 rpm for 10 min, washed with ultrapure water, ethanol, and water at intervals until the pH of the supernatant was neutral, and then lyophilized with a freeze-dryer to obtain PLNP@PDA@DMMA.

***In Vivo* Imaging and Therapy.** Female Balb/c nude mice (5−6 weeks) were purchased from Changzhou Cavens Laboratory Animal Co. Ltd. All experimental protocols were permitted by the Animal Ethics Committee of Jiangnan University, and all operations were conducted strictly in accordance with the guidelines of the Wuxi Committee of Use and Care of Laboratory Animals. The tumor-bearing mouse model was established by subcutaneous injection of SCC-7 cells (1×10^7 cells) into the abdomen of the left forelimb of nude mice. *In vivo* imaging and chemo-PTT therapy were carried out when the tumor diameter reached about 6 mm.

The tumor-bearing mice were divided into two groups randomly for intravenous injection of PLNP@PDA (4 mg mL^{-1}, 200 μL) or PLNP@PDA@DMMA (4 mg mL^{-1}, 200 μL). The dual-wavelength luminescence imaging maps of the mice were gathered at different time points (0.5, 1, 2, 3, 4, 6, 8, 10, 12, and 24 h, respectively) on an IVIS Lumina III imaging system. The mice were pre-excited for 2 min with a 650 nm LED lamp before each image was collected. The mice were euthanized and dissected at 24 h postinjection to investigate the distribution of PLNP in the main organ after different treatments. After digestion with concentrated nitric acid, the content of gallium was determined by inductively coupled plasma mass spectrometry.

For *in vivo* chemo-PTT synergic therapy, SCC-7 tumor-bearing mice were randomly divided into six groups with three mice in each group. The specific information was as follows: group a, no treatment; group b, PBS + 808 nm laser; group c, PLNP@PDA@DMMA (4 mg mL^{-1}, 200 μL in PBS); group d, PLNP@PDA@DMMA/DOX (4 mg mL^{-1}, 200 μL in PBS); group e, PLNP@PDA@DMMA + 808 nm laser (4 mg mL^{-1}, 200 μL in PBS); group f, PLNP@PDA@DMMA/DOX + 808 nm laser (4 mg mL^{-1}, 200 μL in PBS). Groups b, e, and f were irradiated with a 808 nm laser (1 W cm^{-1}) for 10 min at 6 h after injection. The tumor volume and weight of the mice were recorded every day for a total of 3 times for 12 days. The tumor volume was defined as length (cm) × (width)^2 (cm^2)/2.

■ RESULTS AND DISCUSSION

Preparation and Characterization of the Dual-Emissive PLNP. The preparation and surface functionalization of PLNP $ZnGa_2O_4$:Cr for *in vivo* tumor-targeting imaging

and imaging-guided precision chemo-PTT therapy are illustrated in Figure 1. A surfactant-aided hydrothermal
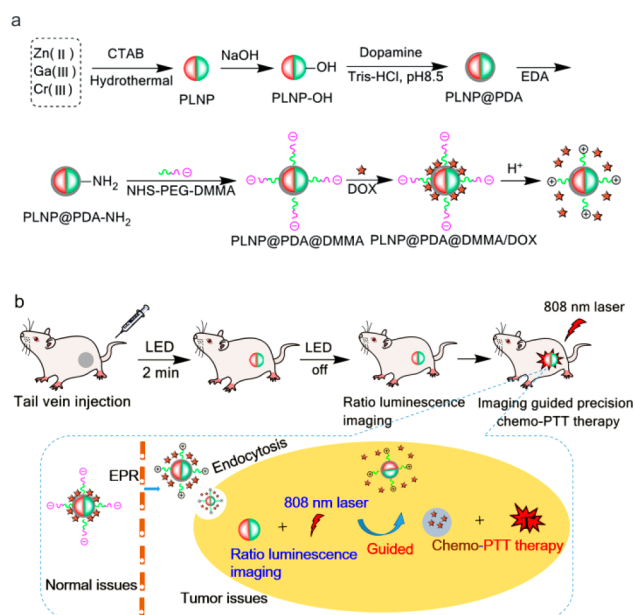

Figure 1. (a) Schematic for the design and synthesis of PLNP@PDA@DMMA/DOX; (b) Illustration of PLNP@PDA@DMMA/DOX as a charge-reversible intelligent theranostic nanoprobe for tumor-targeting ratio imaging and chemo-PTT synergetic therapy.

method in combination with a postcalcination was used to prepare the dual-emissive PLNP by careful control of the content of chromium and the hydrothermal and calcination conditions (Figures S1–S8). The size and crystal structure of the PLNPs were studied using transmission electron microscopy (TEM) (Figures S3, S5, and S7) and X-ray powder diffraction (XRD) (Figures S2 and S8).

Controlling the content of chromium and the hydrothermal and calcination conditions is important for the preparation of the dual-emissive PLNPs. There is a large spectral overlap between the emission band of the zinc gallate matrix and the absorption band from the d–d inner shell transitions of Cr^{3+}, which can result in a transfer of the energy absorbed by the zinc gallate matrix to Cr^{3+}.[28] Therefore, we optimized the doped content of Cr^{3+} first. An increase of Cr^{3+} content enhanced the luminescence at 714 nm but reduced that at 508 nm (Figure S1). However, the Cr^{3+} content had no remarkable influence on the crystal structure and particle size (Figures S2 and S3). The hydrothermal reaction time had a slight effect on the luminescence, persistent afterglow, and particle size of $ZnGa_2O_4$:Cr (Figures S4 and S5). The sintering temperature was further investigated because it can affect not only the number and the depth of the trap but also the transformation of a complete phase to the cubic spinel structure.[29] An increase in sintering temperature enhanced the luminescence at 714 nm in the range of 600–1000 °C. In contrast, the luminescence at 508 nm was the highest at 600 °C but was reduced at sintering temperatures higher than 600 °C (Figure S6). In addition, a higher sintering temperature led to larger particle sizes of the PLNPs (Figure S7). Excellent dual-emissive PLNPs without obvious agglomeration were synthesized with a moderate Cr content ($ZnGa_2O_4$:$Cr_{0.0001}$) and a short hydrothermal time (220 °C, 24 h) in combination with low-temperature calcination (600 °C, 1 h). The as-prepared PLNPs with the

nominal formula $ZnGa_2O_4$:$Cr_{0.0001}$ were well-dispersed and homogeneous square particles with a particle size of 17.37 ± 1.57 nm (randomly calculated from 100 particles) (Figure 2a) and a pure spinel phase of $ZnGa_2O_4$ (Figure 2b) were obtained. The hydrodynamic diameter was 85.9 ± 31.0 nm with a polydispersity index (PDI) of 0.171 (Figure 2a).
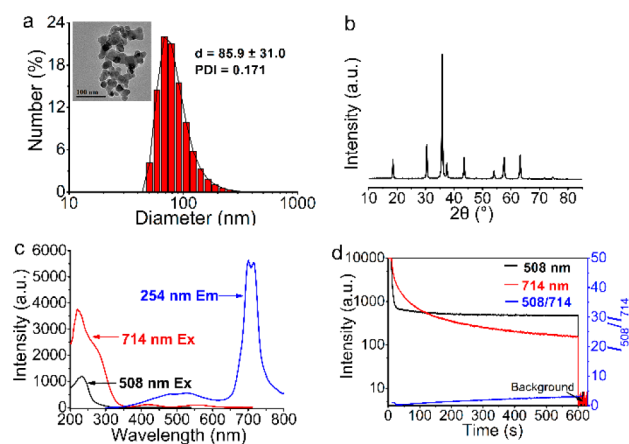
Figure 2. Structural characterization and luminescence properties of the as-synthesized $ZnGa_2O_4$:Cr: (a) hydrodynamic diameter distribution and TEM image (inset); (b) XRD pattern; (c) excitation (emission at 508 and 714 nm) and emission (excitation at 254 nm) spectra; (d) afterglow decay curves and the luminescence ratio curve for the emissions at 508 and 714 nm after 254 nm UV irradiation for 5 min.

Luminescence Properties of the Prepared PLNPs. The as-prepared PLNPs gave two characteristic emission peaks (Figure 2c). One emission peak at 714 nm results from the $^2E \rightarrow {}^4A_2$ transition of twisted Cr^{3+} in the zinc gallate crystal,[30,31] and the other at 508 nm originates from the natural defects in the zinc gallate matrix.[31] The excitation spectrum for the 714 nm emission shows three bands covering a wide spectral region from 200 to 630 nm. The band at 221 nm originates from a combination of the host excitation band and the O–Cr charge transfer band, while the other two bands at 417 and 558 nm result from the d–d inner-shell transition of Cr^{3+} corresponding to $^4A_2 \rightarrow {}^4T_1$ (te^2) and $^4A_2 \rightarrow {}^4T_2$ (t^2e) transitions, respectively.[32,33] The $^4A_2 \rightarrow {}^4T_2$ (t^2e) transition is the primary reason for the reactivation by a LED lamp after irradiation.[34] The excitation spectrum for the 508 nm emission has one band covering from 200 to 300 nm originating from the zinc gallate matrix.[35]

The luminescence of the two emission peaks decayed rapidly but was still detected up to 60 min after excitation stopped (Figure 2d and Figure S9). In addition, the persistent luminescence can be reactivated with both a red LED lamp and 254 nm UV irradiation (Figure 3a,b and Figure S9). Although the persistent luminescence of each emission decreased significantly with time, the ratio of the persistent luminescence intensities for the two emission peaks (I_{508}/I_{714}) was generally stable even after reactivation (Figure 3a,b), effectively avoiding the great variation of luminescence with time in single-emissive PLNPs. The above results show that the prepared reactivatable PLNPs show tremendous promise in long-term persistent luminescence ratio sensing and bioimaging. Moreover, the prepared PLNPs also gave a constant I_{508}/I_{714} ratio signal in *in vivo* imaging even after five repeated reactivations by a red LED lamp (Figure 3c–3f and Figure
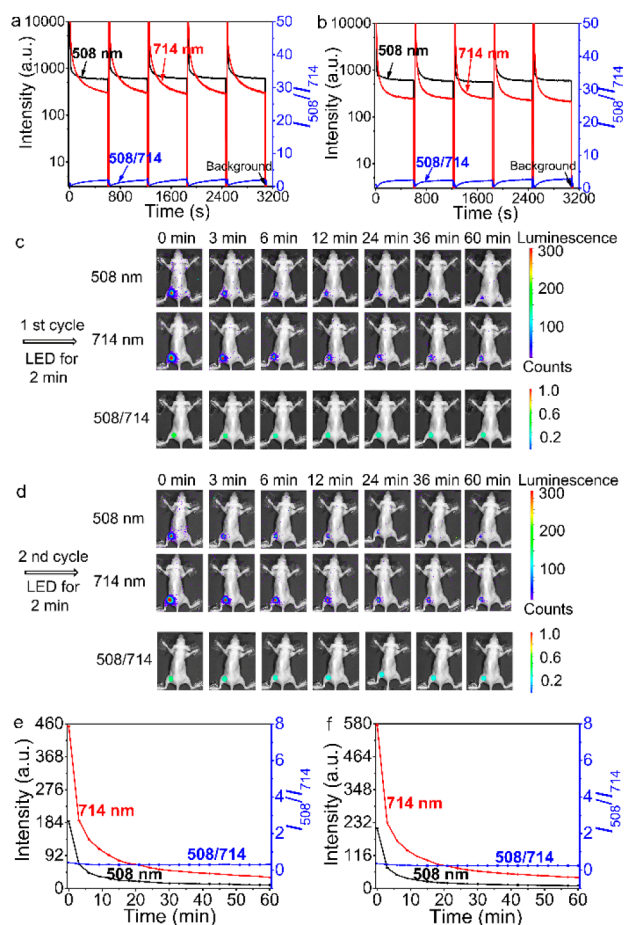
Figure 3. Luminescence properties of the as-synthesized $ZnGa_2O_4$:Cr: luminescence decay curves at 508 nm (black line) and 714 nm (red line) and the ratio intensity curve (blue line) under (a) 254 nm UV lamp reactivation and (b) 650 nm LED lamp reactivation; (c) *in vivo* luminescence images and (d) images of Balb/c nude mice after injection with $ZnGa_2O_4$:Cr (4 mg mL^{-1}, 200 μL) after the reactivation with LED light irradiation for the first and second cycles (the images for the third to fifth reactivations are shown in Figure S10); (e) corresponding *in vivo* luminescence intensity curves and the ratio intensity curve from (c); (f) corresponding *in vivo* luminescence intensity curves and the ratio intensity curve from (d).

S10), ensuring the tremendous potential for long-term precision *in vivo* luminescence ratio imaging.

Preparation and Characterization of PLNP@PDA@ DMMA/DOX. The excellent persistent luminescence ratio imaging performance encouraged us to employ the synthesized PLNPs to establish an intelligent theranostic nanoprobe for tumor-targeting ratio imaging along with a chemo-PTT synergic therapy. To this end, the PLNP was hydroxylated to prepare PLNP-OH, and then a PDA layer was coated onto the surface of the PLNP-OH by the self-aggregation of dopamine as a PTT agent. The reaction time was optimized because of the effect of the near-infrared absorption of PDA on both the luminescence of PLNP and the photothermal conversion ability (Figures S11 and S12). The reaction time of 1 h was selected as a compromise between the photothermal effect and the luminescence intensity. EDA was bonded to the surface of PDA by a Michael addition and/or a Schiff base reaction to obtain PLNP@PDA-NH$_2$. NHS-PEG-DMMA was then introduced onto the surface of PLNP@PDA via a condensation reaction between the −NH$_2$ group of PLNP@PDA-

NH$_2$ and the active ester group of NHS-PEG-DMMA to prolong blood circulation and endow intelligent charge-reversible targeting ability. DOX·HCl was loaded onto PLNP@PDA@DMMA via π−π stacking and electrostatic adsorption, which shows a drug loading efficiency of 4.53%.

The prepared PLNP@PDA@DMMA/DOX had a particle size of 18.44 ± 1.60 nm (randomly calculated from 100 particles) and a hydrodynamic diameter of 131.4 ± 35.1 nm (PDI = 0.195) (Figure 4a). Meanwhile, the ζ potential of
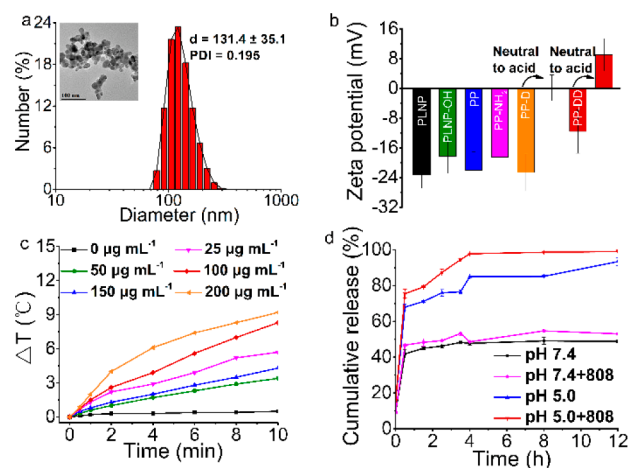

Figure 4. Characterization of PLNP@PDA@DMMA/DOX: (a) hydrodynamic diameter distribution and TEM image (inset); (b) ζ potentials of PLNP, PLNP-OH, PLNP@PDA (denoted PP), PLNP@PDA-NH$_2$ (denoted PP-NH$_2$), PLNP@PDA@DMMA (denoted PP-D), and PLNP@PDA@DMMA/DOX (denoted PP-DD); (c) photothermal performance of PLNP@PDA@DMMA/DOX at various concentrations (pH 7.4) irradiated by an 808 nm laser at a power density of 1.0 W cm^{-2} for 10 min; (d) pH and 808 nm laser mediated *in vitro* DOX release from PLNP@PDA@DMMA/DOX with or without 808 nm laser irradiation (1 W cm^{-2}) for 10 min at 37 °C in the dark. Data are given as mean ± sd (n = 3).

PLNP@PDA@DMMA/DOX changed from −11.60 ± 5.88 mV under neutral conditions to 9.02 ± 4.35 mV under acidic conditions, indicating a charge reversal target ability due to the acid-induced cleavage of DMMA (Figure 4b). PLNP@PDA@ DMMA/DOX showed a typical peak of DOX in FT-IR spectra (Figure S13) and UV−vis spectra (Figure S14). In addition, the synthesized PLNP@PDA@DMMA/DOX gave an spinel phase like that of the PLNPs (Figure S15) and emission spectra similar to those of the PLNPs but a lower luminescence intensity in comparison to the PLNPs owing to the lower proportion of PLNPs in the composite (Figure S16). As such, the smart theranostic nanoprobe PLNP@PDA@DMMA/ DOX was successfully fabricated.

Photothermal Performance and Cytotoxicity of PLNP@PDA@DMMA/DOX. The photothermal performance of PLNP@PDA@DMMA/DOX was determined by irradiating with an 808 nm NIR laser (1.0 W cm^{-2}) for 10 min to investigate the potential for photothermal therapy. The temperature of the PLNP@PDA@DMMA/DOX solution increased with its concentration as well as the 808 nm laser irradiation time (Figure 4c and Figure S17). DOX release was carried out at pH 5.0 and 7.4 to imitate the acidic tumor microenvironment and the normal physiological environment, respectively. Totals of 93.4% and 48.8% of DOX in PLNP@ PDA@DMMA/DOX were released at pH 5.0 and pH 7.4

without irradiation in 12 h, respectively. In contrast, 99.6% and 53.1% of DOX were released at pH 5.0 and pH 7.4 under irradiation with an 808 nm lamp for 10 min (1 W cm^{-2}), respectively (Figure 4d). The results indicate that the photothermal effect of PDA under irradiation speeded up the release of DOX to enhance the antitumor effects and reduce the side effects of the drugs.

The cytotoxicity of PLNP@PDA@DMMA/DOX was evaluated with SCC-7 and 3T3 cells. The dark cytotoxicity of PLNP@PDA@DMMA/DOX and important intermediates (PLNP, PLNP@PDA, and PLNP@PDA@DMMA) toward the two kinds of cells were first evaluated by an MTT assay. The cell viability of the cells about treated with important intermediates remained ca. 90% within the 24 h coincubation even at a test concentration up to 200 μg mL^{-1}, indicating no obvious dark cytotoxicity of the as-prepared PLNP and intermediate (Figure 5a). However, for PLNP@PDA@
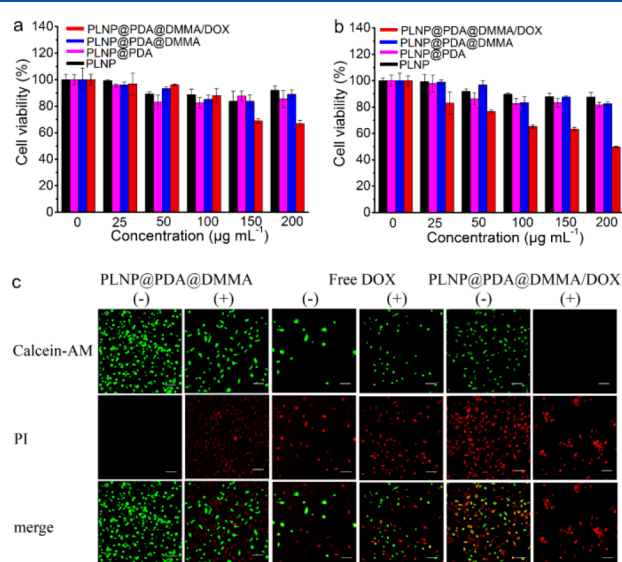
Figure 5. *In vitro* cytotoxicity of PLNP, PLNP@PDA, PLNP@PDA@DMMA, and PLNP@PDA@DMMA/DOX for 3T3 cells (a) and SCC-7 cells (b). Data are given as the mean ± sd (*n* = 5). (c) CLSM images of SCC-7 cells incubated with PLNP@PDA@DMMA, free DOX, and PLNP@PDA@DMMA/DOX with or without 808 nm laser irradiation (1 W cm^{-2} for 10 min) ("−" is defined as no irrradiation with the 808 nm laser and "+" as irradiation with the 808 nm laser). Scale bar: 120 μm. Live cells were stained with Calcein-AM in green, and dead cells were stained with PI in red.

DMMA/DOX up to 100 μg mL^{-1} there was weak cytotoxicity toward SCC-7 cells, likely due to the endocytosis of cancer cells and the release of DOX (Figure 5b).

PLNP@PDA@DMMA/DOX for Bioimaging along with Chemo-PTT Therapy. The cell internalization and targeting imaging capabilities of PLNP@PDA@DMMA were then investigated. For this purpose, 150 μg mL^{-1} of PLNP@PDA@DMMA or PLNP@PDA were incubated with the above cells, respectively, and cell imaging was carried out with a confocal laser scanning microscope (CLSM). The fluorescence of SCC-7 cells incubated with PLNP@PDA@DMMA increased with time, reached a maximum at 6 h, and was always brighter than that of SCC-7 cells treated with PLNP@PDA and 3T3 cells incubated with PLNP@PDA@DMMA or PLNP@PDA (Figures S18−S21). These results indicate that the introduction of NHS-PEG-DMMA contributed to the

enhancement of the tumor-targeting ability and 6 h was the most appropriate incubation time for the following therapy experiment.

The chemo-PTT synergetic therapy efficiency of PLNP@PDA@DMMA/DOX was evaluated on SCC-7 cells. PLNP@PDA@DMMA/DOX irradiated with an 808 nm laser exhibited obvious cytotoxicity (less than 10% cell viability) against SCC-7 cells in a concentration-dependent manner (Figure S22). In contrast, PLNP@PDA@DMMA/DOX without 808 nm laser irradiation and free DOX with or without 808 nm laser irradiation gave less than half of the above cell inhibition rate. The results of a Calcein-Am/PI staining experiment are consistent with those mentioned above (Figure 5c). The above results clearly confirm that PLNP@PDA@DMMA/DOX has excellent chemo-PTT synergistic therapeutic effects.

We then applied PLNP@PDA@DMMA/DOX for *in vivo* tumor-targeting persistent luminescence imaging guided chemo-PTT therapy. The *in vivo* imaging performance was first investigated via intravenous injection of PLNP@PDA@DMMA and PLNP@PDA as the experimental group and control group, respectively. The two-wavelength luminescence signals were observed on the tumor area of the experimental group at ca. 2 h and gradually increased to a maximum at ca. 6 h. Meanwhile, the luminescence signal was clear up to ca. 24 h (Figure 6a). In contrast, almost no luminescence signal was observed in the tumor area of the control group during the whole process. These results indicate that PLNP@PDA@DMMA has great potential for *in vivo* tumor-targeting imaging and 6 h postinjection with maximum accumulated amount was the most appropriate time point for the follow-up therapy.

The tumor-bearing mice were sacrificed and dissected at 24 h post intravenous injection to more intuitively observe the tumor-targeted accumulation and biological distribution of PLNP@PDA@DMMA and PLNP@PDA (Figure S23). Although a luminescence signal was inevitable in the strong phagocytosis of reticuloendothelial system organs (such as lung and liver), an obvious luminescence signal only existed in the tumor site of the mice injected with PLNP@PDA@DMMA, which further illustrated that PEG-DMMA did play a role in enhancing the tumor-targeting accumulation. Moreover, the amount of Ga element in both tumor tissues and major organs (derived from the PLNP core) was measured by inductively coupled plasma mass spectrometry (ICP-MS) to further confirm the tumor-targeting accumulation of PLNP@PDA@DMMA (Figure S24). The quantitative results were highly consistent with the *in vivo* imaging results, confirming that PLNP@PDA@DMMA has good potential for tumor-targeting imaging.

The *in vivo* chemo-PTT synergistic therapeutic effect of PLNP@PDA@DMMA/DOX was then studied. For this purpose, SCC-7 tumor-bearing mice were randomly divided into six groups. SCC-7 tumor-bearing mice (experimental group) were injected with PLNP@PDA@DMMA/DOX and irradiated with an 808 nm laser for 10 min (1 W cm^{-2}) at 6 h postinjection. The other five groups were used as controls: without treatment, injected with PBS and irradiated with an 808 nm laser, treated with PLNP@PDA@DMMA with or without 808 nm laser irradiation, and treated with PLNP@PDA@DMMA/DOX only.

The tumor volume in the PLNP@PDA@DMMA group increased exponentially as did those of the untreated and PBS + 808 nm laser treatment groups, while the tumor tissue was
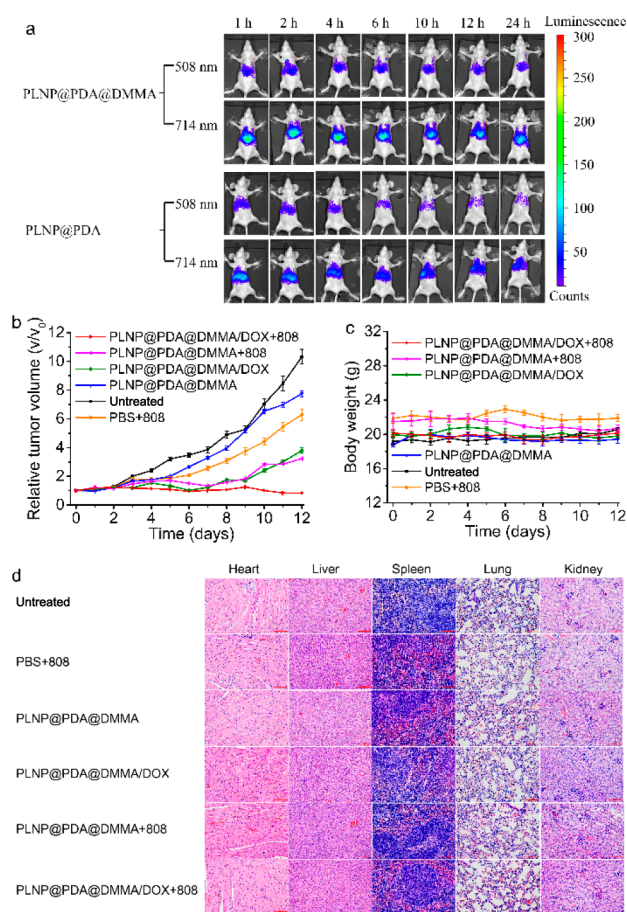
Figure 6. PLNP@PDA@DMMA/DOX-mediated *in vivo* luminescence ratio images and chemo-PTT therapy of SCC-7 tumor-bearing mice: (a) *in vivo* persistent luminescence imaging and ratio imaging of SCC-7 tumor-bearing mice after injection with PLNP@PDA@DMMA or PLNP@PDA irradiated with a 650 nm LED lamp for 2 min before each acquisition; (b) relative tumor volume changes and (c) body weight changes of SCC-7 tumor-bearing mice with different treatments within 12 days; (d) H&E staining of the main organs of SCC-7 tumor-bearing mice after the treatment.

significantly suppressed in the experimental group. Although the tumors for PLNP@PDA@DMMA with 808 nm laser irradiation and PLNP@PDA@DMMA/DOX alone control groups were also suppressed to a certain extent, the inhibition effect was far worse than that of the experimental group, indicating the excellent synergistic chemo-PTT therapy of PLNP@PDA@DMMA/DOX. (Figure 6b and Figure S25). In addition, neither significant body weight changes nor remarkable damage to the main organs was observed in both the experimental and control groups (Figure 6c,d). The above results fully confirm that the developed PLNP@PDA@DMMA/DOX theranostic platform is competent for tumor-specific ablation without obvious side effects, showing good application prospects.

CONCLUSIONS

In summary, we have reported a surfactant-assisted hydrothermal method in combination with postcalcination for the controllable preparation of dual-emissive monodispersed PLNPs ($ZnGa_2O_4$:Cr). The prepared PLNPs emit two luminescence peaks at 508 and 714 nm with a constant luminescence ratio (I_{508}/I_{714}) for more than 1 h after UV

excitation stops. Significantly, the prepared PLNPs give a constant I_{508}/I_{714} ratio signal under the repeated activation by a LED lamp in both *in vitro* and *in vivo* imaging, allowing luminescence ratio imaging to ensure the long-term accuracy for *in vivo* imaging. We have also designed and fabricated a theranostic nanoprobe with intelligent tumor-targeted imaging and chemo-PTT synergistic therapy, which further indicates the unique advantage of the prepared PLNPs for luminescence ratio imaging guided therapy. We believe that the dual-emissive PLNPs will provide a promising nanoplatform for imaging and for diagnosis applications.

ASSOCIATED CONTENT

Supporting Information

The Supporting Information is available free of charge at https://pubs.acs.org/doi/10.1021/acs.analchem.1c01220.

Materials and chemicals, characterization, DOX loading and release, other experimental procedures, and additional figures as described in the text (PDF)

AUTHOR INFORMATION

Corresponding Authors

Xu Zhao − *State Key Laboratory of Food Science and Technology, International Joint Laboratory on Food Safety, and Institute of Analytical Food Safety, School of Food Science and Technology, Jiangnan University, Wuxi 214122, People's Republic of China;* orcid.org/0000-0001-8000-9045; Email: zhaoxu2017@jiangnan.edu.cn

Xiu-Ping Yan − *Key Laboratory of Synthetic and Biological Colloids, Ministry of Education, School of Chemical and Material Engineering, State Key Laboratory of Food Science and Technology, International Joint Laboratory on Food Safety, and Institute of Analytical Food Safety, School of Food Science and Technology, Jiangnan University, Wuxi 214122, People's Republic of China;* orcid.org/0000-0001-9953-7681; Phone: +86-510-85916732; Email: xpyan@jiangnan.edu.cn

Authors

Jia-Lin Liu − *Key Laboratory of Synthetic and Biological Colloids, Ministry of Education, School of Chemical and Material Engineering and Institute of Analytical Food Safety, School of Food Science and Technology, Jiangnan University, Wuxi 214122, People's Republic of China*

Li-Jian Chen − *State Key Laboratory of Food Science and Technology, International Joint Laboratory on Food Safety, and Institute of Analytical Food Safety, School of Food Science and Technology, Jiangnan University, Wuxi 214122, People's Republic of China;* orcid.org/0000-0001-8671-8766

Lu-Ming Pan − *Key Laboratory of Synthetic and Biological Colloids, Ministry of Education, School of Chemical and Material Engineering and Institute of Analytical Food Safety, School of Food Science and Technology, Jiangnan University, Wuxi 214122, People's Republic of China*

Complete contact information is available at:
https://pubs.acs.org/10.1021/acs.analchem.1c01220

Notes

The authors declare no competing financial interest.

ACKNOWLEDGMENTS

REFERENCES

(1) Civit, L.; Pinto, A.; Rodrigues-Correia, A.; Heckel, A.; O'Sullivan, C. K.; Mayer, G. *Methods* **2016**, *97*, 104−109.

(2) Bagó, J. R.; Sheets, K. T.; Hingtgen, S. D. *Methods* **2016**, *99*, 37−43.

(3) Sun, X.; Lei, Y. *TrAC, Trends Anal. Chem.* **2017**, *89*, 163−180.

(4) Vahrmeijer, A. L.; Hutteman, M.; van der Vorst, J. R.; van de Velde, C. J. H.; Frangioni, J. V. *Nat. Rev. Clin. Oncol.* **2013**, *10*, 507−518.

(5) Hayata, Y.; Kato, H.; Konaka, C.; Ono, J.; Takizawa, N. *Chest* **1982**, *81*, 269−277.

(6) Nseyo, U. O.; DeHaven, J.; Dougherty, T. J.; Potter, W. R.; Merrill, D. L.; Lundahl, S. L.; Lamm, D. L. *J. Clin. Laser Med. Surg.* **1998**, *16*, 61−68.

(7) Qu, B.; Zhang, B.; Wang, L.; Zhou, R.; Zeng, X. C. *Chem. Mater.* **2015**, *27*, 2195−2202.

(8) Maldiney, T.; Lecointre, A.; Viana, B.; Bessière, A.; Bessodes, M.; Gourier, D.; Richard, C.; Scherman, D. *J. Am. Chem. Soc.* **2011**, *133*, 11810−11815.

(9) Abdukayum, A.; Yang, C. X.; Zhao, Q.; Chen, J. T.; Dong, L. X.; Yan, X. P. *Anal. Chem.* **2014**, *86*, 4096−4101.

(10) Shi, J.; Sun, X.; Zhu, J.; Li, J.; Zhang, H. *Nanoscale* **2016**, *8*, 9798−9804.

(11) Wu, B. Y.; Wang, H. F.; Chen, J. T.; Yan, X. P. *J. Am. Chem. Soc.* **2011**, *133*, 686−688.

(12) Harizaj, A.; Clercq, O.; Descamps, B.; Vanhove, C.; Smedt, C.; Poelman, D.; Lentacker, I.; Braeckmans, K. *Part. Part. Syst. Charact.* **2019**, *36*, 1900371.

(13) Li, Y. J.; Yang, C. X.; Yan, X. P. *Anal. Chem.* **2018**, *90*, 4188−4195.

(14) Laxman, K.; Reddy, B. P. K.; Mishra, S. K.; Gopal, M. B.; Robinson, A.; De, A.; Srivastava, R.; Ravikanth, M. *ACS Appl. Mater. Interfaces* **2020**, *12*, 52329−52342.

(15) Huang, X.; El-Sayed, I. H.; Qian, W.; El-Sayed, M. A. *J. Am. Chem. Soc.* **2006**, *128*, 2115−2120.

(16) Xu, J.; Yang, P.; Sun, M.; Bi, H.; Liu, B.; Yang, D.; Gai, S.; He, F.; Lin, J. *ACS Nano* **2017**, *11*, 4133−4144.

(17) Valastyan, S.; Weinberg, R. A. *Cell* **2011**, *147*, 275−292.

(18) Veiseh, O.; Kievit, F. M.; Ellenbogen, R. G.; Zhang, M. *Adv. Drug Delivery Rev.* **2011**, *63*, 582−596.

(19) Tian, G.; Zhang, X.; Gu, Z.; Zhao, Y. *Adv. Mater.* **2015**, *27*, 7692−7712.

(20) Fan, W.; Bu, W.; Shi, J. *Adv. Mater.* **2016**, *28*, 3987−4011.

(21) Wang, X. Y.; Zhang, J. S.; Wang, Y. T.; Wang, C. P.; Xiao, J. R.; Zhang, Q.; Cheng, Y. Y. *Biomaterials* **2016**, *81*, 114−124.

(22) Pasparakis, G.; Manouras, T.; Vamvakaki, M.; Argitis, P. *Nat. Commun.* **2014**, *5*, 3623.

(23) Che, H.; van Hest, J. C. M. *J. Mater. Chem. B* **2016**, *4*, 4632−4647.

(24) Chien, Y. H.; Chou, Y. L.; Wang, S. W.; Hung, S. T.; Liau, M. C.; Chao, Y. J.; Su, C. H.; Yeh, C. S. *ACS Nano* **2013**, *7*, 8516−8528.

(25) Du, J. Z.; Sun, T. M.; Song, W. J.; Wu, J.; Wang, J. *Angew. Chem., Int. Ed.* **2010**, *49*, 3621−3626.

(26) He, W.; Zheng, X.; Zhao, Q.; Duan, L.; Lv, Q.; Gao, G. H.; Yu, S. *Macromol. Biosci.* **2016**, *16*, 925−935.

(27) Lee, Y.; Fukushima, S.; Bae, Y.; Hiki, S.; Ishii, T.; Kataoka, K. *J. Am. Chem. Soc.* **2007**, *129*, 5362−5363.

(28) Bessière, A.; Jacquart, S.; Priolkar, K.; Lecointre, A.; Viana, B.; Gourier, D. *Opt. Express* **2011**, *19*, 10131−10137.

(29) Yan, S.; Wang, J.; Gao, H.; Wang, N.; Yu, H.; Li, Z.; Zhou, Y.; Zou, Z. *Adv. Funct. Mater.* **2013**, *23*, 1839−1845.

(30) Pan, Z.; Lu, Y. Y.; Liu, F. *Nat. Mater.* **2012**, *11*, 58−63.

(31) Bessière, A.; Sharma, S. K.; Basavaraju, N.; Priolkar, K. R.; Binet, L.; Viana, B.; Bos, A. J. J.; Maldiney, T.; Richard, C.; Scherman, D.; Gourier, D. *Chem. Mater.* **2014**, *26*, 1365−1373.

(32) Abdukayum, A.; Chen, J. T.; Zhao, Q.; Yan, X. P. *J. Am. Chem. Soc.* **2013**, *135*, 14125−14133.

(33) Li, Y.; Geceviciusa, M.; Qiu, J. R. *Chem. Soc. Rev.* **2016**, *45*, 2090−2136.

(34) Maldiney, T.; Bessiere, A.; Seguin, J.; Teston, E.; Sharma, S. K.; Viana, B.; Bos, A. J. J.; Dorenbos, P.; Bessodes, M.; Gourier, D.; Scherman, D.; Richard, C. *Nat. Mater.* **2014**, *13*, 418−426.

(35) Binet, L.; Gourier, D. *J. Phys. Chem. Solids* **1998**, *59*, 1241−1249.